**Accurate modeling of the dynamics of dissociative chemisorption on metal surfaces**
Gerrits, N.

## Citation

Gerrits, N. (2021, September 23). *Accurate modeling of the dynamics of dissociative chemisorption on metal surfaces*. Retrieved from https://hdl.handle.net/1887/3213516

# Chapter 7

# CHD$_3$ + Cu(111), Cu(211), and Single-Atom Cu(111) Alloys

# Abstract

In order to model accurately reactions of polyatomic molecules with metal surfaces important for heterogeneous catalysis in industry, the Specific Reaction Parameter (SRP) approach to density functional theory has been developed. This approach has been shown to describe the dissociation of CHD$_3$ on Ni(111), Pt(111), and Pt(211) with chemical accuracy. In this work, predictions have been made for the reaction of CHD$_3$ on Cu(111) and Cu(211) using barriers, elbow plots, and Born-Oppenheimer molecular dynamics. Hopefully, future experiments can prove the transferability of the SRP density functional to systems in which methane reacts with flat and stepped surfaces of adjacent groups of the periodic table, by comparison with the present predictions. Moreover, the effect of a so-called single atom alloy on the reactivity of methane is investigated by making predictions for CHD$_3$ on Pt–Cu(111) and Pd–Cu(111). It is found that the reactivity is only increased for Pt–Cu(111) near the alloyed atom, which is not only caused by the lowering of the barrier height but also by changes in the dynamical pathway and reduction of energy transfer from methane to the surface.

## 7.1   Introduction

For heterogeneous catalysis, one of the most important processes is steam reforming, where methane and steam react over a metal catalyst and form molecular CO and hydrogen. At high temperatures, the dissociation of methane is a rate controlling step on a wide variety of metals[1, 2], and thus warrants detailed study of the breaking of the CH bond on metal surfaces. Moreover, methane dissociation on copper is a much investigated method for creating high quality graphene[3–9]. However, due to the complexity of the interaction between metals and molecules and of describing both metals and molecules accurately, this reaction remains difficult for theoretical studies[10–14]. Recently, it has been shown that chemically accurate results can be obtained for molecule-metal surface reactions by using a so-called Specific Reaction Parameter (SRP) approach[15–17]. Furthermore, the recently developed SRP32-vdW density functional (DF) not only gives chemically accurate results for the reaction for which it is developed (CHD₃ + Ni(111)[16]), but it is also transferable to systems in which methane interacts with metals from the same group (CHD₃ + Pt(111)[17]) and with stepped surfaces of the same metal (CHD₃ + Pt(211)[17]). In this chapter predictive calculations are performed for the reaction of methane on surfaces of a metal belonging to a neighbouring group of the periodic table, in the hope that these predictive calculations will be followed by experiments that can test the transferability of the SRP32-vdW DF to methane interacting with a flat and stepped Cu surface, i.e., Cu(111) and Cu(211).

Moreover, a way to improve catalysts is to introduce alloys[18], which can be used to both increase reactivity and selectivity[19]. For example, methane dissociation is so highly activated on Pt and Ni that the methane will completely dehydrogenate and thus poison the catalyst[20–22]. However, by combining Pt or Ni with a less reactive metal like Cu, a highly active catalyst that does not poison itself can be produced[22]. In order to be able to clearly identify the effect of the different metals, so-called Single Atom Alloys (SAA) are investigated in this chapter, where a small portion (5%) of the top surface atoms is replaced with a different metal. These alloyed metal atoms do not cluster and thus can be viewed as single isolated atoms[23–25]. So far only a limited amount of information is available for the reaction of methane on alloys[22, 26–30]. As such, the SRP32-vdW DF will not only be used to make a prediction for Cu(111) and Cu(211), but it will also be applied to SAAs of Cu(111) that incorporate metals for which the DF either gives chemically accurate results (Pt), or is expected to do so (Pd).

In short, in this chapter a prediction is made for the reactivity of CHD₃

on Cu(111), Cu(211), Pd-Cu(111) and Pt-Cu(111). Furthermore, a detailed analysis of the dynamical behaviour is provided. This chapter is structured as follows: a short summary of the technical details is given in Section 7.2. The barriers are discussed in Section 7.3.1 followed by the minimum energy path in Section 7.3.2. In Section 7.3.3 the sticking probabilities are presented, while Section 7.3.4 concerns the impact site associated with reactive collisions. Finally, a short summary is given in Section 7.4.

## 7.2  Method

All the Born-Oppenheimer molecular dynamics (BOMD) and electronic structure (Density Functional Theory, DFT) calculations have been performed with the Vienna Ab-initio Simulation Package (VASP version 5.3.5)[31–35]. A kinetic energy cutoff of 350 eV and a $\Gamma$-centered $6 \times 6 \times 1$ *k*-point grid are used. Furthermore, core electrons have been represented with the projector augmented wave (PAW) method[35, 36], using an Ar core PAW pseudo-potential for Cu. The (111) surfaces are modeled using a 5 layer $(3 \times 3)$ supercell, while the (211) surface is modeled using a 4 layer $(1 \times 3)$ supercell. Furthermore, the vacuum distance between the slabs is 13 Å. In order to speed up convergence, first-order Methfessel-Paxton smearing[37] with a width parameter of 0.2 eV has been applied. Calculations have been performed without spin polarization, which is not required for a diamagnetic material as Cu. This computational setup is confirmed to yield results that are converged to within chemical accuracy (1 kcal/mol, or 4.2 kJ/mol), and results with respect to this convergence are given in Section 7.A.

For the alloys, a single surface layer atom in the supercell is replaced with a Pt or Pd atom, which is similar to what is observed in experiment[22, 24], and results in a coverage of $1/9^{\text{th}}$ of a monolayer. The alloyed atom is confirmed to remain at its position, i.e., it does not travel over the surface.

Transition states (TSs) are obtained with the dimer method[38–41] as implemented in the VASP Transition State Tools package (VTST)[42], with the forces on the molecule's atoms converged within 5 meV/Å. The TSs are confirmed to be first-order saddle points by doing a frequency analysis, i.e., by checking if only one imaginary frequency was found. An ideal slab is used, where the top three layers have been relaxed in the *Z* direction.

For the BOMD simulations a surface temperature of 550 K is used, where the atoms in the top three layers are allowed to move in all three directions and the ideal lattice constant is expanded by a factor of 1.0078 in order to reflect the expansion of the bulk due to the surface temperature[43]. The

TABLE 7.1: Experimental beam parameters that describe the simulated CHD$_3$ velocity distributions. The stream velocity ($v_0$) and the width parameter ($\alpha$) are determined through time-of-flight measurements for the nozzle temperatures ($T_n$) of 750 and 900 K[16]. The parameters for $\langle E_i \rangle$ = 181.3 kJ/mol are not from experiment, but theoretical estimates obtained by extrapolation.

| $T_n$ (K) | $\langle E_i \rangle$ (kJ/mol) | $v_0$ (m/s) | $\alpha$ (m/s) |
|---|---|---|---|
| 750 | 136.4 | 3760.72 | 216.91 |
| 900 | 160.4 | 4070.12 | 274.51 |
| 1050* | 181.3 | 4320.12 | 324.01 |

frequency $\omega$ employed in the 1D harmonic oscillator model for the simulation of surface atom motion (see Section 2.4.1 for this procedure) is in the range of $1.4 < \omega < 1.8$ kJ/mol. Ten differently-initialized slabs are generated using the aforementioned procedure, resulting in a pool of 10 000 snapshots. The average temperature of the pool of snapshots is $(541 \pm 60)$ K. For every BOMD data point, 1000 trajectories were run, unless noted otherwise, with a time step of 0.4 fs. The rest of the technical details for the BOMD calculations can be found in recent work[16, 17, 44] and in Chapter 2.

The initial translational energy of the molecules has been sampled from the experimental molecular beam parameters (stream velocity and width parameter), which are provided in Table 7.1. Experiments for $\langle E_i \rangle$ = 181.3 kJ/mol were not readily available, so parameters were estimated. Moreover, the nozzle temperature is merely an estimate of what is needed to obtain a beam with the required translational energy distribution, but for the state population this is not an issue since at this energy BOMD was only done for CHD$_3$ in the single rovibrational state it would be excited to in a laser-on experiment. The residual energy $E_R$ (1.9 kJ/mol) is added to the kinetic energy in order to correct for the interaction with the periodic image and reduced plane wave cutoff energy, as is described in Sections 2.4.2 and 7.A. The laser-off beams are simulated by sampling the initial vibrational states of the molecule from a Boltzman distribution at $T_n$, while its initial angular momentum has been set to zero and the molecule's orientation is randomly sampled. The $v_1 = 1$ and $v_1 = 2$ beams are simulated by initializing all molecules with one or two quanta in the CH stretch mode, respectively. Moreover, the experimental R(1) transition to the rotational state $J = 2$ and $K = 0$ is simulated in the BOMD trajectories (see Section 2.4.2 for the simulation of the rotational states). The alignment in $M$ should be erased by hyperfine coupling due to the long pathway of the excited molecules in the experiments[12]. Therefore, $M$ has

been statistically sampled, i.e., $M = -2, -1, 0, 1, 2$ with equal probability.

The SRP32-vdW DF is employed, which was previously used for $CHD_3$ + Ni(111), Pt(111) and Pt(211)[16, 17], of which the exchange part is defined as

$$E_x = x \cdot E_x^{\text{RPBE}} + (1 - x) \cdot E_x^{\text{PBE}}, \tag{7.1}$$

where $E_x^{\text{RPBE}}$ and $E_x^{\text{PBE}}$ are the exchange parts of the RPBE and PBE[45, 46] exchange-correlation DFs, respectively, and $x = 0.32$. Moreover, the vdW correlation DF of Dion and coworkers (vdW-DF1)[47] is used. Earlier work has shown that using a Van der Waals correlation DF may be important to a correct description of the energy dependence of the reaction probability[48], signifying that the variation of the barrier height with molecular orientation and impact site is correctly described[48], and that this is also true for methane interacting with metals[16, 17, 49]. With the use of an appropriate correlation DF and an appropriate weighted average of exchange DFs, SRP-DFT has been shown capable of accurately describing the minimum barrier height, the anisotropy and corrugation of the barrier height, and the position of the barrier, which determines how efficiently pre-exciting stretch vibrations may enhance the reactivity (see Ref. [15] and the supporting information of Refs. [16] and [50]). Finally, $CHD_3$ is used instead of $CH_4$ in order to avoid artificial intramolecular vibrational energy redistribution (IVR) in the dynamics when the CH stretch mode is vibrationally excited[44, 51]. For arguments regarding the reliability of the quasi-classical trajectory (QCT) approach implicit in the BOMD, the reader is referred to the supporting information of Refs. [16] and [44]. There, the authors were able to argue that the QCT approach should not suffer much from problems like zero-point energy violation, and be accurate already for reaction of molecules in their ground vibrational state just above the reaction threshold, with reaction probabilities of the order of a percent. This was established on the basis of the quality of the comparison of QCT calculations with quantum dynamics calculations for $D_2$ + Cu(111)[52], as $D_2$ has a similar vibrational frequency and reduced mass as the CH stretch vibration in $CHD_3$, and of actual BOMD calculations for $CHD_3$ + Pt(111) which showed that the reaction near the threshold only involved zero-point energy violation in only 1 out of 144 reactive trajectories[44].

TABLE 7.2: Barrier geometries for CHD$_3$ + Cu(100), Cu(111), Cu(211), Pt-Cu(111), Pd-Cu(111), Pd(111), Ni(111) and Pt(111). The naming convention from Ref. [53] is used for the (100) and (111) surfaces. Geometry names for Cu(211) indicate first the location of the methane and then the direction of the dissociating H atom. The height of the C atom on Cu(211) is taken with respect to the top step edge (EtoE and E/BtoB geometries) or to the middle of the (111) terrace (TtoB geometry). For $\theta$, $\beta$ and $\gamma$ on Cu(211), the surface normal is taken as the macroscopic surface normal. The zero-point energy corrected barriers are given in the brackets. The calculations are performed with the SRP-vdW-DF1 DF, unless indicated otherwise.

| Surface | Site | $Z_C$ (Å) | $r$ (Å) | $\theta$ (°) | $\beta$ (°) | $\gamma$ (°) | $E_b$ (kJ/mol) |
|---|---|---|---|---|---|---|---|
| Cu(100) | G2 geometry | 2.19 | 1.84 | 129.4 | 165.3 | 35.9 | 166.1 (152.1) |
| Cu(111) | C2 geometry | 2.25 | 1.79 | 136.4 | 169.4 | 33.0 | 166.6 (151.8) |
| Cu(111) | C2 geometry (550 K) | 2.25 | 1.80 | 136.6 | 168.4 | 31.9 | 167.9 (153.4) |
| Cu(111) | C2 geometry (PBE-vdW) | 2.24 | 1.77 | 136.3 | 168.3 | 32.0 | 157.2 (143.1) |
| Cu(111) | C2 geometry (optB86b-vdW) | 2.19 | 1.74 | 134.1 | 167.5 | 33.4 | 136.2 (122.4) |
| Cu(111) | C2 geometry (optB86b-vdW)[22] | - | - | - | - | - | 129.3 |
| Cu(111) | C2 geometry (SRP32-DF2) | 2.28 | 1.79 | 137.1 | 168.8 | 31.7 | 182.3 (167.8) |
| Cu(111) | Fcc | 2.25 | 1.80 | 133.4 | 162.5 | 29.2 | 187.4 (171.7) |
| Cu(111) | Bridge | 2.26 | 1.84 | 129.8 | 160.8 | 31.0 | 193.9 (178.2) |
| Cu(211) | EtoE geometry | 2.08 | 1.86 | 125.1 | 157.4 | 34.4 | 137.8 (128.4) |
| Cu(211) | E/BtoB geometry | 1.90 | 1.81 | 158.3 | 168.3 | 33.4 | 152.9 (138.8) |
| Cu(211) | TtoB geometry | 1.39 | 1.81 | 143.1 | 163.2 | 33.3 | 174.3 (159.8) |
| Pt-Cu(111) | Atop Pt | 2.36 | 1.66 | 133.2 | 165.3 | 32.1 | 134.1 (121.8) |
| Pt-Cu(111) | Atop Pt (PBE-vdW) | 2.35 | 1.65 | 132.7 | 164.9 | 32.2 | 124.8 (112.6) |
| Pt-Cu(111) | Atop Pt (optB86b-vdW) | 2.32 | 1.62 | 131.4 | 164.2 | 32.9 | 100.3 (88.1) |
| Pt-Cu(111) | Atop Pt (optB86b-vdW)[22] | - | - | - | - | - | 84.9 |
| Pt-Cu(111) | Nearest neighbour | 2.26 | 1.83 | 137.5 | 170.3 | 32.8 | 173.4 (159.2) |
| Pt-Cu(111) | Next nearest neighbour | 2.26 | 1.80 | 136.3 | 168.7 | 32.5 | 165.7 (151.8) |
| Pt-Cu(111) | Next nearest neighbour (PBE-vdW) | 2.21 | 1.79 | 135.7 | 168.2 | 32.5 | 156.4 (143.3) |
| Pt-Cu(111) | Next nearest neighbour (optB86b-vdW) | 2.16 | 1.76 | 133.4 | 167.4 | 34.0 | 135.6 (122.4) |
| Pd-Cu(111) | Atop Pd | 2.32 | 1.76 | 136.9 | 167.9 | 32.0 | 142.5 (129.2) |
| Pd-Cu(111) | Nearest neighbour | 2.26 | 1.81 | 136.7 | 169.0 | 32.4 | 172.3 (158.0) |
| Pd-Cu(111) | Next nearest neighbour | 2.25 | 1.80 | 136.2 | 168.7 | 32.5 | 167.6 (153.5) |
| Ni(111) | C2 geometry[16] | 2.18 | 1.61 | 135.7 | 164.7 | 29.1 | 97.9 (85.3) |
| Pd(111) | A2 geometry | 2.23 | 1.61 | 135.9 | 165.0 | 29.1 | 84.6 (70.7) |
| Pt(111) | D1 geometry[17] | 2.28 | 1.56 | 133 | 168 | 35 | 78.7 (66.5) |
| Pt(111) | D1 geometry (PBE-vdW)[49] | 2.29 | 1.54 | 133.9 | 168.4 | - | 73.9 (61.7) |
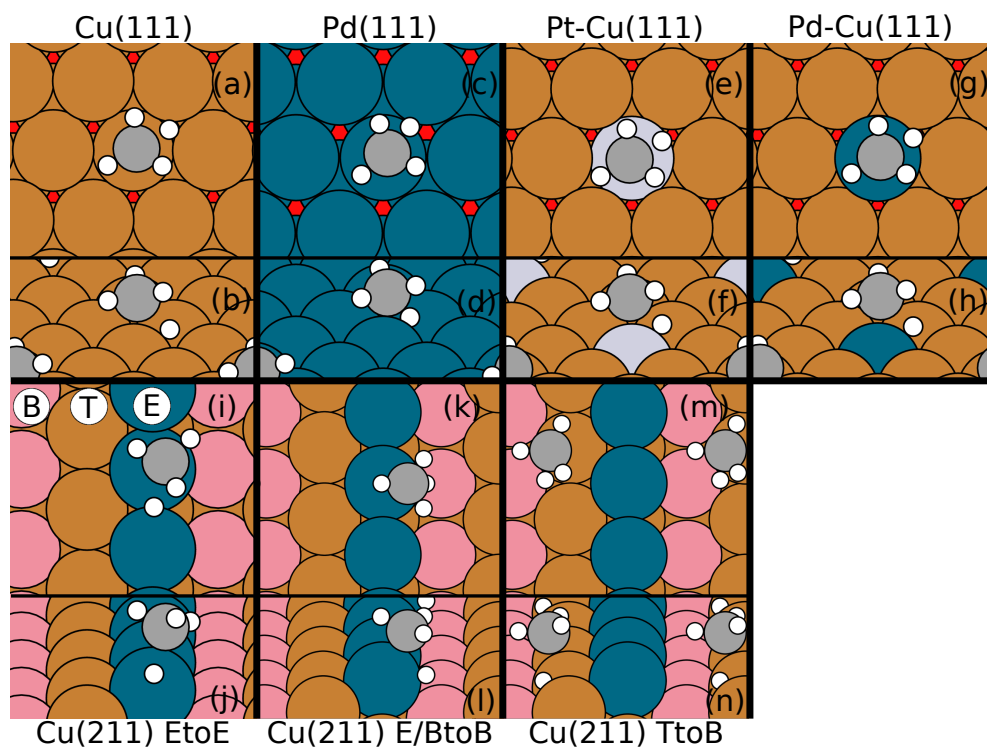
FIGURE 7.1: Top and side view of the TS of methane on Cu(111) with the C2 geometry (a,b); Pd(111) with the A2 geometry (c,d); on Pt-Cu(111) (e,f) and Pd-Cu(111) (g,h) with the C2 geometry; and on Cu(211) with the EtoE (i,j), E/BtoT (k,l), and TtoT (m,n) geometries. For the (111) surfaces, red indicates the fcc sites. For Cu(211), pink indicates the bottom step edge atoms (B), orange the terrace atoms (T), and blue the top step edge atoms (E).
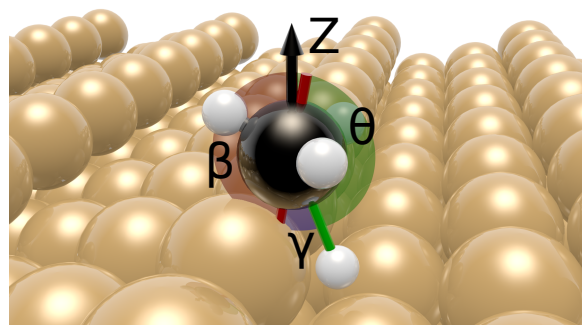


FIGURE 7.2: Methane on Cu(211) with the E/BtoB geometry, indicating the geometry angles as used in Table 7.2. $\theta$ is the angle between the dissociating CH-bond and the surface normal, $\beta$ is the angle between the umbrella axis and the surface normal, and $\gamma$ is the angle between $\theta$ and $\beta$.

## 7.3    Results

### 7.3.1    Activation Barriers and Adsorption Energies

The TS geometries for the dissociation of methane on several surfaces are summarized in Table 7.2 and in Figure 7.1, where the naming convention from Ref. [53] is used for the TSs on the (100) and (111) surfaces. Figure 7.2 depicts the angles that are used to characterize the TSs. $\theta$ is the angle between the surface normal and the dissociating CH bond and $\beta$ is the angle between the surface normal and the umbrella axis, which is defined as the vector going from the geometric center of the three H-atoms to the carbon atom. Finally, $\gamma$ is the angle between the dissociating CH bond and the umbrella axis.

The TS geometry on Cu(111) is similar to Ni(111) and Pt(111), except the CH-bond and umbrella axis of the methane have a slightly smaller tilt with respect to the surface normal (i.e., $\theta$ and $\beta$ are larger) and the bond distance ($r^{\ddagger}$) of the dissociating hydrogen is much larger; i.e., the location of the barrier is later compared to Ni(111) and Pt(111). Moreover, the barrier height is 166.6 kJ/mol, which is 68.7 kJ/mol higher than for Ni(111). Since the barrier on Cu(111) is later and higher than on Ni(111) and Pt(111), less reactivity is expected. The barrier geometry does not change considerably when PBE-vdW is used instead of SRP32-vdW, but the barrier height is 9.4 kJ/mol lower. This is to be expected since PBE is less repulsive than a mixture of PBE and RPBE[15]. Likewise, the barrier height increases only with 1.3 kJ/mol when the expanded lattice constant for 550 K is used, and the barrier geometry does not change considerably. Again, using vdW-DF2[54] instead of vdW-DF1 has little effect on the geometry, although it does increase the barrier height by 15.7 kJ/mol. However, using optB86b-vdW[55] does not only lower the barrier by 30.2 kJ/mol, it also makes the methane tilt more with respect to the surface and shortens the length of the dissociating bond, making the barrier slightly earlier. The barrier height with optB86b-vdW is in good agreement with previous work[22], being 6 kJ/mol higher when the barrier is adjusted for an adsorption well of 13 kJ/mol (the barriers in previous work were reported with respect to the physisorbed state).

The barriers on the fcc and bridge sites are found by fixing the $X$ and $Y$ coordinates of the carbon atom at these sites. While these barriers are second order saddle points, they do provide additional insight on the reactivity across the surface. The CH-bond length is longer and the methane is tilted more compared to the top site, and the barrier height is 20.8 and 27.3 kJ/mol higher for the fcc and bridge site, respectively. The barrier height on Cu(100) is similar to the barrier height on Cu(111), which has been observed previously[5].

TABLE 7.3: Adsorption energy of $CH_3$ on Cu(111). The naming convention for the geometries is from Ref. [53].

| Site | $Z_C$ (Å) | Adsorption energy (kJ/mol) |
|------|-----------|----------------------------|
| Bridge2 | 0.48 | -154.8 |
| Bridge3 | 0.48 | -154.1 |
| Fcc1 | 0.48 | -154.1 |
| Fcc2 | 0.48 | -140.6 |
| Hcp1 | 0.48 | -154.8 |
| Hcp2 | 0.48 | -141.6 |
| Top1 | 0.49 | -150.3 |
| Top2 | 0.49 | -150.4 |
| Top3 | 0.49 | -150.5 |

TABLE 7.4: Adsorption energy of H on Cu(111).

| Site | $Z_H$ (Å) | Adsorption energy (kJ/mol) |
|------|-----------|----------------------------|
| Bridge | 0.44 | -234.5 |
| Fcc | 0.44 | -245.3 |
| Hcp | 0.44 | -244.9 |
| Top | 0.47 | -196.4 |

Furthermore, the methane molecule has a larger tilt and is closer to the Cu(100) surface, while the barrier is slightly later. These differences between the (100) and (111) surfaces are observed for Ni as well[56], except that the barrier height is 15 kJ/mol lower on Ni(100) than on Ni(111).

Tables 7.3 and 7.4 show the adsorption energies for $CH_3$ and H on Cu(111), with the naming convention for the adsorption geometries from Ref. [53]. For the adsorption energies, calculations were done with spin polarization. Methyl adsorbs stronger on the hollow and bridge sites than on the top site. Moreover, the adsorption is stronger when the hydrogen atoms are oriented towards the top sites, than towards the hollow sites. Finally, the hollow sites are the most favorable adsorption site for hydrogen, followed by the bridge and top sites. These results are in agreement with earlier theoretical results[5].

For Cu(211), three distinctly different barriers are found: above the top step edge atom, between the top and bottom step edge, and on the terrace, which are referred to as the EtoE, E/BtoB and TtoB geometries, respectively. In

general, the length of the dissociating CH bond is larger than on Cu(111), i.e., the barriers for Cu(211) are even later than for Cu(111). Furthermore, the barrier on the terrace (TtoB geometry) is 7.7 kJ/mol higher than on Cu(111), while the barriers at the step (EtoE and E/BtoB geometries) are 28.8 and 13.7 kJ/mol lower, respectively. Finally, for the EtoE geometry the hydrogen dissociates towards the bridge site, which is at odds with the other TS geometries obtained on Cu(211) for which the hydrogen atom moves towards a hollow site.

For alloys, above the next nearest neighbour Cu atom, almost no changes are observed compared to Cu(111). The nearest neighbour Cu atom shows an almost identical barrier geometry, but above these Cu atoms the barrier heights for Pt-Cu(111) and Pd-Cu(111) are 7 and 6 kJ/mol higher than on Cu(111), respectively. However, above the alloyed top atoms the barrier changes considerably. The barrier above Pt is further away from the surface and the dissociating CH bond distance is smaller than for Cu(111), although the barrier is later than on Pt(111). Moreover, the barrier height is reduced with 32.7 kJ/mol relative to Cu(111), although the barrier is much higher than on Pt(111). When using another DF like PBE-vdW, these changes to the barrier are very similar, suggesting that mixing PBE with RPBE only affects the minimum barrier height and not other physics like the energetic corrugation of the barrier height. This finding is in agreement with a similar finding in quantum Monte Carlo and DFT calculations on $H_2$ + Al(110)[57]. Previous work[22] using the optB86b-vdW DF reported a much larger reduction of 44 kJ/mol relative to Cu(111), whereas here a reduction of 35.7 kJ/mol is found when using the optB86b-vdW DF. However, the barrier heights previously reported[22] were incorrect and the corrected results are available in Ref. [58]. The geometry found previously[22] is slightly different, but can only explain a small part of the difference (about 2 kJ/mol) between previous results and results in this work. Most of the difference is caused by the relaxation of the surface atoms during the dimer calculation in Ref. [22] due to the considerable resulting protrusion of the Pt atom. Furthermore, using a different XC-DF (optB86b-vdW[55]) results in smaller lattice constants for solids[59]. This could mean that due to different lattice constants caused by the different DFs, a different strain in the lattice of a SAA is observed, resulting in a different barrier height for the alloy.

Marcinkowski et al.[22] introduced the parameter

$$\alpha = \frac{E_b^{Cu(111)} - E_b^{Pt\text{-}Cu(111)\,(atop\,Pt)}}{E_b^{Cu(111)} - E_b^{Pt(111)}}, \tag{7.2}$$

where $\alpha = 0$ and $\alpha = 1$ indicate a barrier height equal to Cu(111) and Pt(111),

respectively. The lower barrier found previously[22] gives $\alpha_{optB86b\text{-}vdW} = 0.52$, i.e., the barrier is almost halfway between a Pt(111)-like and Cu(111)-like barrier, whereas the higher barrier found in this work with the SRP32-vdW DF is closest to Cu(111), i.e., $\alpha_{SRP32\text{-}vdW} = 0.37$. Moreover, PBE-vdW also results in a more Cu(111)-like barrier with $\alpha_{PBE\text{-}vdW} = 0.39$. Although additional work is needed, it seems that by allowing the Pt atom to pucker out, the barrier becomes more Pt-like for Pt-Cu(111).

Finally, it is checked that relaxing the top layer also in the *X* and *Y* directions does not have a large influence on the barrier height. When the top layer is also relaxed in the *X* and *Y* directions before the dimer calculation (but note that the top layer is kept fixed during the TS search), above Pt the barrier height is further reduced by 3.4 kJ/mol and above the next nearest neighbour Cu the barrier height is increased by 1.2 kJ/mol. It is expected that similarly small effects will occur for the case of Pd-Cu(111).

Above the alloyed Pd top atom in Pd-Cu(111) the barrier height is reduced by 24.1 kJ/mol and the changes for the geometry relative to Cu(111) are similar as for the Pt alloy, but smaller. This is to be expected, since the barrier height on Pd(111) is also higher and later than on Pt(111). Likewise, Pd-Cu(111) has a barrier height that is even more similar to a Cu(111)-like barrier height since $\alpha = 0.29$, which is also reflected by the fact that the barrier geometry above Pd is more similar to that found on Cu(111) than what is observed above Pt.

### 7.3.2 Minimum Energy Path

Figure 7.3a shows the minimum energy path (MEP) of methane dissociating above the top site on Cu(111). Methane is fixed in its TS geometry, while varying the length of the dissociating CH bond and distance from the surface. Since methane has 15 degrees of freedom, the potential along the MEP will increasingly differ from the true MEP in which other coordinates also vary, when moving away from the TS. However, points from a nudged elastic band[60] (NEB) calculation, where all degrees of freedom are relaxed, in Figure 7.3a are in excellent agreement with the MEP, and this is assumed to be also the case for other surfaces. As already stated above, the barrier is late and high on Cu(111). Moreover, the MEP does not have a smooth curvature, but makes almost a right angle in the elbow plot. Hence, incoming molecules may not be able to follow the MEP due to the requirement of a high kinetic energy to overcome the barrier combined with the sharp turn of the MEP, and thus may have to react over much higher barriers ("*the bobsled effect*"[61, 62]). This can also be seen in Figure 7.3c, where the reacted trajectories at $\langle E_i \rangle = 181.3$ kJ/mol for $\nu_1 = 1$ are superimposed on the elbow plot. Even
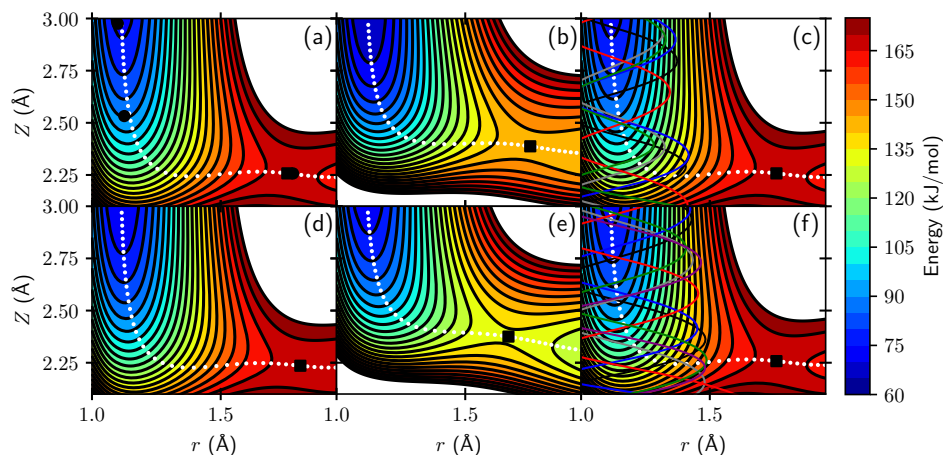
FIGURE 7.3: Elbow plot of methane on Cu(111) (a), above Pd in Pd-Cu(111) (b), above the next nearest neighbour Cu in Pt-Cu(111) (d), and above Pt in Pt-Cu(111) (e). (c) and (f) are the same as (a), but with reacted trajectories for $\langle E_i \rangle = 181.3$ kJ/mol and $\nu_1 = 1$ (c) and $\nu_1 = 2$ (f). Methane is fixed in its TS geometry above the top site, whereas $Z$ and the distance of the dissociating CH-bond are variable. Contour lines are drawn at intervals of 5 kJ/mol between 60 and 180 kJ/mol. The colours indicate the energy (kJ/mol) with respect to methane in the gas phase. The white circles indicate the MEP. The black circles in panel (a) indicate points from a NEB calculation, while the black squares indicate the highest point along the MEP.

when the vibrational energy is increased to $\nu_1 = 2$ the trajectories are not able to follow the MEP in Figure 7.3f. Nevertheless, the trajectories do approach the minimum TS more closely when the vibrational energy is increased (see Chapter 8), but this effect is not visible in Figures 7.3c,f. Furthermore, in Figure 7.4 the top site TS geometry is taken and used to plot the PES for methane above the fcc site resulting in a similar elbow plot, although the MEP is more strongly curved. The barrier obtained from this elbow plot is 185.9 kJ/mol, which is only 1.5 kJ/mol lower than the barrier obtained using a constrained dimer search. This suggests that the barrier geometry is almost independent of the reaction site. Additionally, the change in energy when moving away from the TS at the top site is similar to the change found at the fcc site, i.e., the corrugation around the barrier geometry is again almost independent of the reaction site.

Similarly, Figure 7.3b shows the MEP of methane dissociating above the Pd atom in Pd-Cu(111). Here, the MEP is further away from the surface and through a lower barrier than for Cu(111). However, the MEP above the Pt
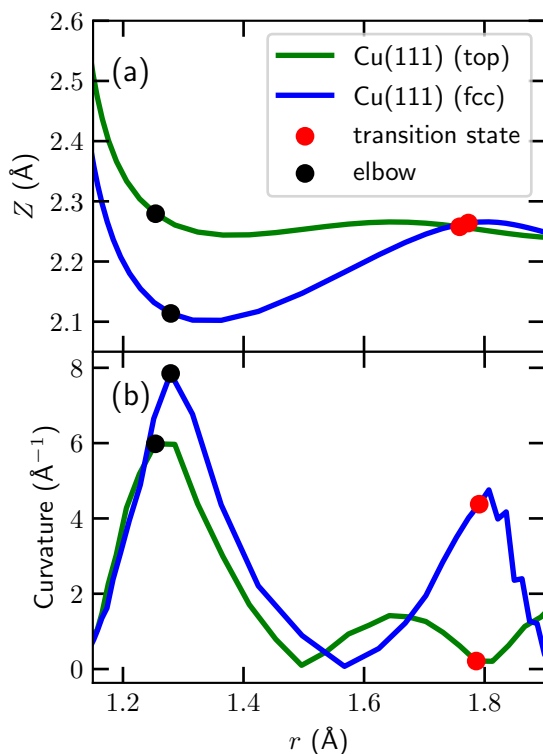
FIGURE 7.4: (a) The MEP from Figure 7.3a (green) and above the fcc site on Cu(111) (blue). The fcc PES and concomitant MEP is obtained by placing the top site TS geometry above the fcc site. (b) Curvature from the afore-mentioned MEPs. The red points indicate the TS, while the black squares indicate the point on the MEP with the largest curvature.

atom in Pt-Cu(111) in Figure 7.3e shows larger differences than above Pd relative to Cu(111), which could be caused by the fact that the barrier above Pd is more similar to Cu(111) than above Pt. Above Pt the barrier is lower and earlier and the MEP has a smoother curvature. Furthermore, the MEP for Pt-Cu(111) has a similar curvature, although at a higher distance to the surface, as the MEP for Pt(111) does, while the barrier is later and higher. Above the next nearest Cu atom for both alloys a similar MEP was obtained as for Cu(111), as can be seen in Figure 7.3e for Pt-Cu(111). Summarizing, the MEPs above the Pt and Pd atoms in the alloys exhibit similar, but not identical features as the MEPs for Pt(111) and Pd(111). Above the Cu atoms in the alloys the MEPs are similar to the MEP for Cu(111).

The MEP of methane above the step edge of Cu(211) in Figure 7.5a is similar to that for Cu(111) in Figure 7.3a, although closer to the surface. Moreover, the barrier is lower, but later. Figure 7.5c shows the same elbow plot, but here the $\theta$ coordinate is also optimized. The turn the MEP makes for the optimized $\theta$ is slightly smoother early on, but as soon as the bond starts extending the
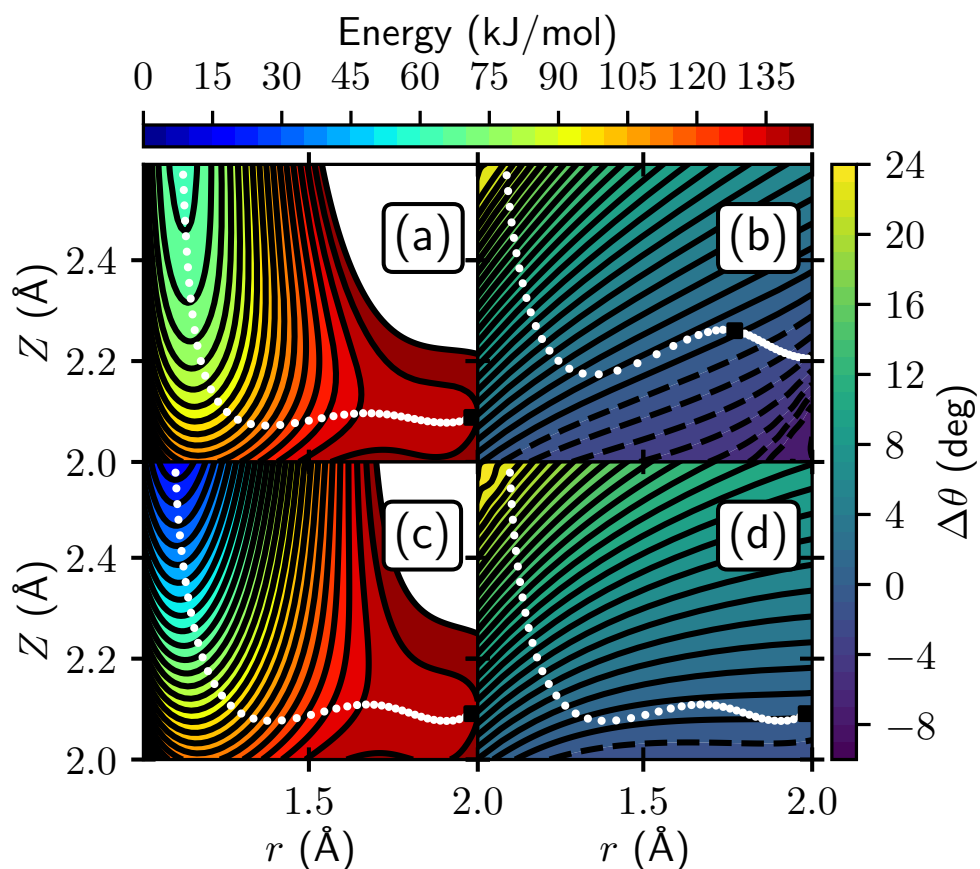
FIGURE 7.5: Same as figure 7.3, but for Cu(211) with the EtoE geometry (a) and with the $\theta$ angle optimized (c). (b) and (d) show the MEP for Cu(111) and Cu(211), where $\theta$ is optimized. The contour lines in (a) and (c) are drawn at intervals of 5 kJ/mol between 0 and 150 kJ/mol and indicate the energy (kJ/mol) with respect to methane in the gas phase. The colours in (b) and (d) indicate the difference in angle with respect to the TS, and contour lines are drawn at intervals of 0.5 degrees between -10 and 24 degrees. The black squares indicate the highest point along the MEP.

curvature actually increases compared to the case where $\theta$ is kept fixed, i.e., from the curvature point of view the MEP becomes dynamically less favorable compared to the MEP for which $\theta$ is not optimized. The difference in $\theta$ with respect to the TS for which the energy is minimized is shown in Figures 7.5b and 7.5d. If the molecule would follow the MEP, it would undergo a rapid reorientation of the CH-bond when it approaches the surface before it is able to extend the CH bond. The bending along the MEP for Cu(211) is similar as for Cu(111).

### 7.3.3   Sticking Probability

In Table 7.5 results are summarized for BOMD on several surfaces. At incidence energies close to the minimum barrier height, methane has a much lower sticking probability on Cu(111) than on Ni(111). At $\langle E_i \rangle = 160 \, \text{kJ/mol}$ and $v_1 = 1$ no reaction is observed on Cu(111), and with $v_1 = 2$ a reaction probability of only 2.4% is obtained. At higher incidence energy some reaction is observed, but only for vibrationally excited molecules, which also explains why only CH cleavage is observed and no CD cleavage.

Surprisingly, on Cu(211) a similar reaction probability is obtained as for Cu(111). This could imply that the lower barriers found around the step edge on Cu(211) are dynamically inaccessible. However, CD cleavage is observed, which could indicate that methane found a lower barrier to dissociate over on Cu(211) than on Cu(111) since no CD cleavage was found at Cu(111) for the same or even higher energy, although it remains unclear whether this is a statistical anomaly. It is more probable that an increase in reactivity due to the steps combined with a reduction in reactivity due to the terraces, leads to a similar reactivity for Cu(211) as Cu(111).

On Pd-Cu(111) the reaction probability is low for $\langle E_i \rangle = 160 \, \text{kJ/mol}$ and $v_1 = 1$, i.e., only $0.1\% \pm 0.1$. Apparently, the lowering of the barrier atop the Pd atom is not large enough to enable the reaction of methane for 160 kJ/mol and $v_1 = 1$. In contrast, on Pt-Cu(111) a higher reaction probability is observed. Interestingly, the barrier atop the Pt atom on Pt-Cu(111) is only 8 kJ/mol lower than atop Pd on Pd-Cu(111), and it is not clear whether this can fully account for the increased reaction probability at $\langle E_i \rangle = 160 \, \text{kJ/mol}$ and for $v_1 = 1$. It is possible that since the barrier on Pt is earlier and the MEP in the entrance channel is less curved than on Pd, the reaction is also dynamically more favorable on the Pt doped surface than on the Pd doped surface due to a smaller bobsled effect[61, 62]. Moreover, it was found that the energy transfer from scattered methane to the surface atoms of Pt-Cu(111) and Pd-Cu(111) surface is about 10 kJ/mol lower than to the Cu(111) surface

TABLE 7.5: Sticking probabilities obtained with BOMD for Cu(111), Cu(211), Pd-Cu(111), Pt-Cu(111) and Ni(111). For Cu(111) and Cu(211) at 160 kJ/mol and $v_1 =$ 1, 500 and 692 trajectories were done, respectively. The error bars represent 68% confidence intervals.

| Surface | $\langle E_i \rangle$ (kJ/mol) | Quantum states | Reaction probability (%) | Fraction CH cleavage |
|---|---|---|---|---|
| Cu(111) | 160.4 | $v_1 = 1$ | 0.0 ± 0.2 | - |
| Cu(111) | 160.4 | $v_1 = 2$ | 2.4 ± 0.5 | 1.00 ± 0.05 |
| Cu(111) | 181.3 | $v_1 = 1$ | 0.5 ± 0.2 | 1.00 ± 0.20 |
| Cu(111) | 181.3 | $v_1 = 2$ | 4.8 ± 0.7 | 1.00 ± 0.02 |
| Cu(211) | 160.4 | $v_1 = 1$ | 0.1 ± 0.1 | 0.00 ± 0.32 |
| Cu(211) | 181.3 | $v_1 = 1$ | 0.4 ± 0.2 | 0.75 ± 0.22 |
| Pd-Cu(111) | 160.4 | $v_1 = 1$ | 0.1 ± 0.1 | 1.00 ± 0.32 |
| Pt-Cu(111) | 160.4 | Laser-off | 0.6 ± 0.2 | 0.00 ± 0.17 |
| Pt-Cu(111) | 160.4 | $v_1 = 1$ | 1.4 ± 0.4 | 0.71 ± 0.12 |
| Ni(111)[16] | 160.4 | Laser-off | 28 ± 2.0 | 0.24 ± 0.05 |
| Ni(111)[16] | 160.4 | $v_1 = 1$ | 41 ± 2.2 | 0.53 ± 0.03 |

TABLE 7.6: Energy transfer (kJ/mol) of scattered methane to Cu(111), Pd-Cu(111), Pt-Cu(111) and Pt(111) at $\langle E_i \rangle = 160 \, \text{kJ/mol}$. The results for Pt(111) are extrapolated from earlier work[17]. The error bars represent 68% confidence intervals.

| Surface | Energy transfer | Refined Baule model |
|---|---|---|
| Cu(111) | $62 \pm 1$ | 68 |
| Pd-Cu(111) | $53 \pm 1$ | 66 |
| Pt-Cu(111) | $52 \pm 1$ | 64 |
| Pt(111)[17] | $28 \pm 1$ | 24 |

at equal incidence energy ($\langle E_i \rangle = 160 \, \text{kJ/mol}$) (see Table 7.6). It is possible that due to the additional lattice strain caused by the alloyed atoms, energy transfer from methane to the surface via phonon excitations is less efficient. This is also supported by the fact that the partial phonon densities of states of the Pt and nearest neighbour Cu top layer atoms in Pt-Cu(111) are found at higher energies than in Cu(111), which is shown in Section 7.C. Furthermore, it is likely that the difference in energy transfer is partially caused by the difference in mass between the Cu atoms and the alloyed atoms, as one would expect in the Baule model[63, 64] (see Section 2.5). A modified Baule model, which weights energy loss to the Pt or Pd atom in the surface layer according to its fractional coverage in the SAA, yields good agreement with the BOMD results for energy transfer to the surface atoms (Table 7.6).

In most cases, exciting the $\nu_1$ vibrational mode leads to more CH-cleavage than CD cleavage (see Table 7.5). However, it remains difficult to draw conclusions on the fraction of CH cleavage due to the limited amount of reacted trajectories. Furthermore, Figure 7.6 shows distributions of the $\theta$, $\beta$ and $\gamma$ angles of methane on Cu(111) and Pt-Cu(111) at the highest collision energies, noting that the initial conditions are similar for the two surfaces, except that methane has a higher kinetic energy and vibrational excitation on Cu(111) than on Pt-Cu(111). Here it can be seen that the angular distributions of the reacting methane are similar on both surfaces and that there is little steering in the $\theta$ and $\beta$ angles, but there is quite some steering in the bend angle $\gamma$ in order to follow the MEP. Moreover, it is to be expected on the basis of the elbow plots that the vibrational efficacy is high. Unfortunately, due to the limited amount of reactivity typically only vibrationally excited molecules react, i.e., vibrational energy promotes the reaction but it is unclear by how much, as laser-off reaction is hardly seen. Therefore, it is not possible not compute vibrational efficacies for the BOMD data computed here. Finally, no trapping is observed, which is to be expected considering the high kinetic
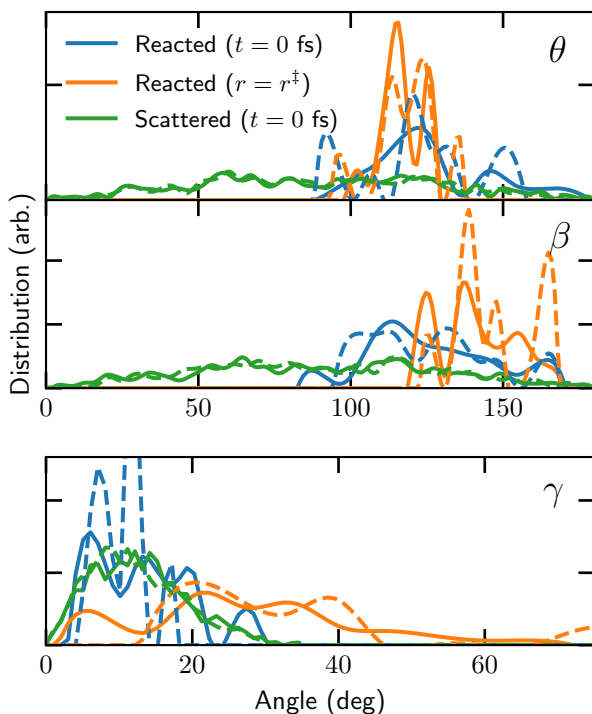
FIGURE 7.6: Distributions of the $\theta$, $\beta$ and $\gamma$ angles of methane during BOMD for scattered (green) and reacted trajectories at the initial time step (blue) and when a dissociating bond reaches the TS value (orange). Solid lines are for Cu(111) ($\langle E_i \rangle$ = 181 kJ/mol and $\nu_1$ = 2) and dashed lines are for Pt-Cu(111) ($E_i$ = 160 kJ/mol and $\nu_1$ = 1).

energy methane has in the performed simulations.

### 7.3.4 Reaction Site

Figures 7.7a,c show the reaction site of methane on Cu(111) for $\nu_1 = 1$ and $\nu_1 = 2$, respectively, with $\langle E_i \rangle = 181$ kJ/mol. Methane does not have a clear preference of reaction site on Cu(111), since the distribution appears to be statistical. It is likely that since the barrier above the hollow sites is only 21 kJ/mol higher than above the top site, and methane has a high energy due to both the translational and the vibrational energy, dynamically there is no preference of reaction site. Also, no significant steering in $X$ and $Y$ is observed for either scattered or reacted trajectories.

On Cu(211) methane reacts only at the step, as can be seen in Figure 7.8. Furthermore, during the dissociation the methyl moves towards the bottom step edge, while the dissociating hydrogen moves towards the terrace, with the dissociating bond located above the top step edge atom. This can also be seen from the fact that the center of mass moves from the top step edge
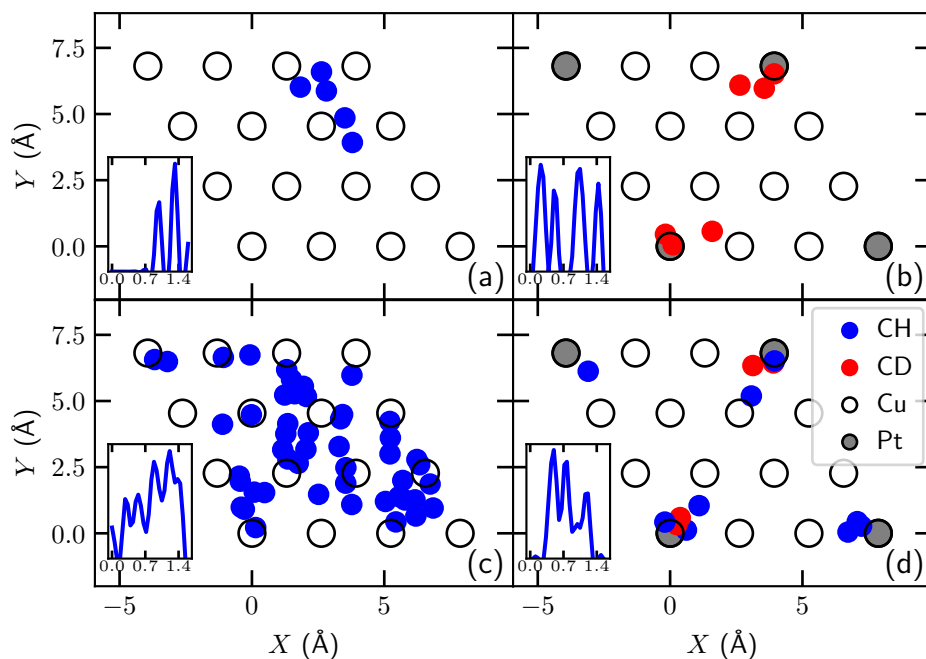
FIGURE 7.7: The impact site of reacting methane on Cu(111) for $\nu_1 = 1$ (a) and $\nu_1 = 2$ (c), with $\langle E_i \rangle = 181$ kJ/mol, and on Pt-Cu(111) for laser-off (b) and laser-on ($\nu_1 = 1$) (d), with $\langle E_i \rangle = 160$ kJ/mol. The grey circles indicate Pt atoms, while the black open circles indicate the Cu top layer surface atoms. The blue (CH cleavage) and red (CD cleavage) circles are the impact sites when dissociation takes place, i.e., when $r = r^{\ddagger}$. The distribution of distance (Å) of the reacting $CHD_3$ to the closest top site (either a Cu or Pt top layer atom) is given in the inset.

FIGURE 7.8:  The impact site of reacting methane on Cu(211) for $\langle E_i \rangle = 181\,\text{kJ/mol}$ and $\nu_1 = 1$. The blue shaded area indicates the step, while the red dashed line is the top step edge. The blue circles are the top layer surface atoms, and the green and red circles are the impact sites where dissociation of a CH (green) or CD (red) bond occurred. The empty green and red circles indicate the location of methane at $t = 0\,\text{fs}$, while the solid circles are for when dissociation takes place, i.e., when $r = r^\ddagger$.
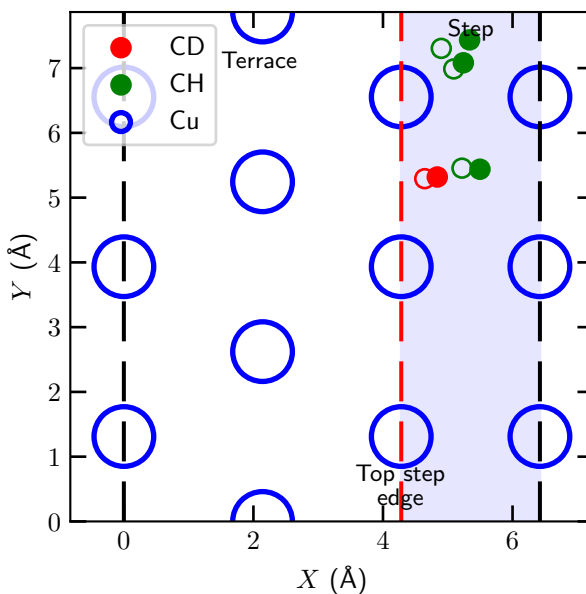


towards the bottom step edge, i.e., there is some steering. Interestingly, for none of the reactive events the center of mass is above the top step edge atom, which is the location of the lowest barrier, nor does the dissociation take place with the hydrogen atom moving towards the bottom step edge, in which case the dissociation would have to proceed over another barrier. Due to the limited amount of reacted trajectories it remains unclear whether this is a statistical anomaly or whether the aforementioned barriers are dynamically inaccessible, for instance due to the late barrier geometry.

On Pt-Cu(111), for both laser-off and laser-on conditions, reaction occurs near the Pt, as can be seen in Figures 7.7b and 7.7d. This means that Pt only alters the barrier locally as suggested by the elbow plots and the minimum barriers. Moreover, in contrast to Cu(111), methane reacts relatively closer to the Pt top site, with no difference being observed between CH and CD bond dissociation. Again, no significant steering in $X$ and $Y$ is observed.

## 7.4    Conclusions

In this chapter predictions have been made with BOMD on the reactivity of methane on several copper-based surfaces using the SRP32-vdW DF, combined with barriers and elbow plots in order to rationalize the results. The results

predict a much lower reactivity for Cu(111) than for Ni(111) and Pt(111) due to the high and late barrier found on Cu(111), requiring high translational and vibrational energies in order to observe reaction. Furthermore, methane has the same reaction probability on Cu(211) as on Cu(111), but with the reaction occurring only at the steps. This can be understood from the lower barriers at the step and higher barriers at the terrace relative to Cu(111). Moreover, making a so-called single-atom alloy from Cu(111) with Pt increases reactivity. This is partially caused by the reduction of the barrier height, together with changes in the dynamical pathway and reduction in energy transfer from the molecule to the surface. The minimum barrier is only affected locally around the alloyed atom, i.e., the Cu surface is unaffected, which is also reflected by the fact that methane only reacts near the top site of the Pt atom. Also, the choice of the exchange-correlation DF can have a large effect on the changes of the local barrier above the alloyed atom. For Pd-Cu(111), the reduction in barrier height and changes in the dynamical pathway were not sufficient to observe reactivity at the same energies as Pt-Cu(111). Finally, it is to be hoped that these predictive calculations will be followed by experiments in order to prove the transferability of the SRP32-vdW DF among systems in which methane interacts with flat and stepped surfaces of metals belonging to adjacent groups of the periodic table, and among systems in which the interaction is with SAAs of these metals.

In this chapter, the predictions of the reactivity of methane on copper surfaces are for a limited range of incidence energies, which additionally are at the high end of what can be achieved with molecular beams using seeding with $H_2$. In chapter 8 a larger range of incidence energies is investigated with a neural network approach, where a potential energy surface is fitted for methane interacting with a mobile copper surface.

# Appendix

## 7.A Electronic Structure Calculations

Convergence tests have been performed to ensure that the aforementioned setup produces accurate results for the interaction of methane with Cu(111). As a convergence test, calculation of the minimum reaction barrier height of $CHD_3$ on Cu(111) has been done. However, the same convergence behavior is expected for other TS geometries, metal surfaces, and exchange-correlation DFs. The barrier height is defined as $E_b = \epsilon_b - \epsilon_{asym}$, where $\epsilon_b$ and $\epsilon_{asym}$ are the absolute energies from the DFT calculations for the barrier geometry and the asymptotic configuration, respectively. The asymptotic configuration is considered to be the gas phase configuration and is obtained by putting the molecule halfway between two periodic slabs, i.e., the distance between the carbon of the methane and the surface is 6.5 Å. The results are presented in Figure 7.A.1. Converged setups yield a barrier height of 168 kJ/mol, which the employed computational setup can reproduce within chemical accuracy (i.e., 4.2 kJ/mol).

The effect of the vacuum distance has also been investigated. When a vacuum distance of 30 Å is employed, while keeping $Z = 6.5$ Å, the residual energy is about 2.5 kJ/mol, where the residual energy is defined as $E_R = E_b^{13\,\text{Å}} - E_{b,Z=6.5\,\text{Å}}^{30\,\text{Å}}$. Furthermore, the barrier height is reduced by 0.6 kJ/mol when using a cutoff energy of 350 eV compared to higher cutoff energies, which is independent of other parameters such as the amount of $k$-points and layers. In order to keep the calculations tractable, a vacuum distance of 13 Å is kept and a cutoff energy of 350 eV is used, but 1.9 kJ/mol is added to the initial kinetic energy during the BOMD (see Section 2.4.2). This is motivated by the fact that the interaction energy at this distance is only dependent on the molecular coordinate $Z$, which is shown in figure 7.A.2. Here methane is kept fixed in its gas phase equilibrium geometry, while varying $Z$ above the top site for a vacuum distance of 13 and 30 Å, where $Z$ is defined as the distance between the surface and the center of mass of methane. The Van der Waals well depth depends on the orientation of the hydrogen atoms, i.e., if more hydrogen atoms point towards the surface, the Van der Waals well is deeper.
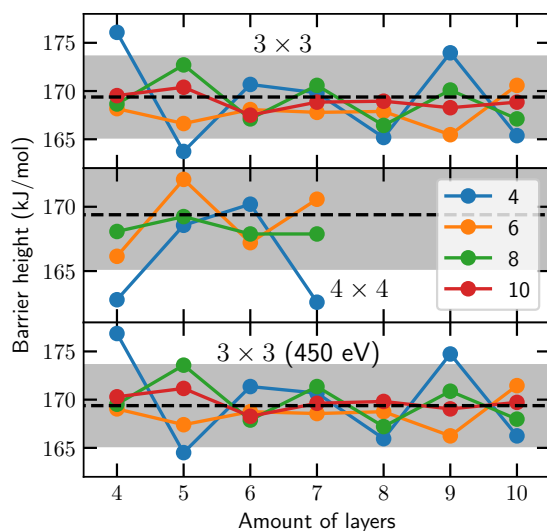
FIGURE 7.A.1: The barrier height as a function of the amount of layers for varying amount of $k$-points ($n \times n \times 1, n = 4, 6, 8, 10$). The first panel is with an energy cutoff of 350 eV and a $3 \times 3$ supercell, second panel is with an energy cutoff of 350 eV and a $4 \times 4$ supercell, and the last panel is with an energy cutoff of 450 eV and a $3 \times 3$ supercell. The dashed lines indicate the converged barrier height and the gray area indicates chemical accuracy (4.2 kJ/mol) with respect to the converged barrier height.

The number $n$ defines the amount of $k$-points and is indicated in the legend.
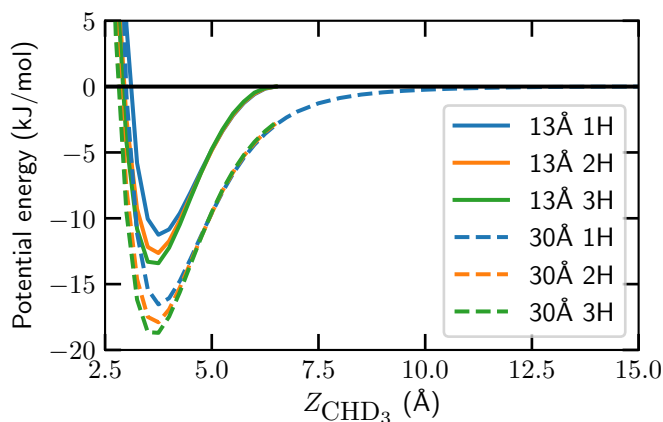
FIGURE 7.A.2: The Van der Waals interaction of methane with a Cu(111) surface as a function of the distance $Z$ between the surface and the methane, with 1 (blue), 2 (orange) or 3 (green) hydrogen atoms pointing towards the surface. The solid and dashed lines indicate results of using a vacuum distance of 13 and 30 Å, respectively. The asymptotic energy is considered to be zero.

The exact orientation and impact site of the molecule have been found not to influence the results for the Van der Waals energy significantly. For 1, 2 and 3 hydrogen atoms pointing towards the surface and a vacuum distance of 13 Å, a Van der Waals adsorption well was found of 12, 13 and 14 kJ/mol, respectively. When the vacuum distance is increased to 30 Å, the physisorption energy is 4.8 kJ/mol higher. Furthermore, the equilibrium distance to the surface is approximately 3.75 Å. These results are comparable to what Li et al. found[6], who found an adsorption energy of 15 kJ/mol and an equilibrium distance for physisorped methane of 3.532 Å.

The described computational setup is used to perform bulk calculations within the primitive unit cell for a fcc lattice, which yielded an equilibrium lattice constant $a_0 = 3.679$ Å, which is 1.8% larger than the experimental value $a_0 = 3.615$ Å[65]. The obtained lattice constant was used to model the Cu(111), Pt-Cu(111), Pd-Cu(111) and Cu(211) slabs.

## 7.B  Minimum Energy Paths

Figure 7.B.1 shows the elbow plot and the MEP of methane on Cu(111) above the fcc site, using the TS geometry obtained above the top site. The MEP
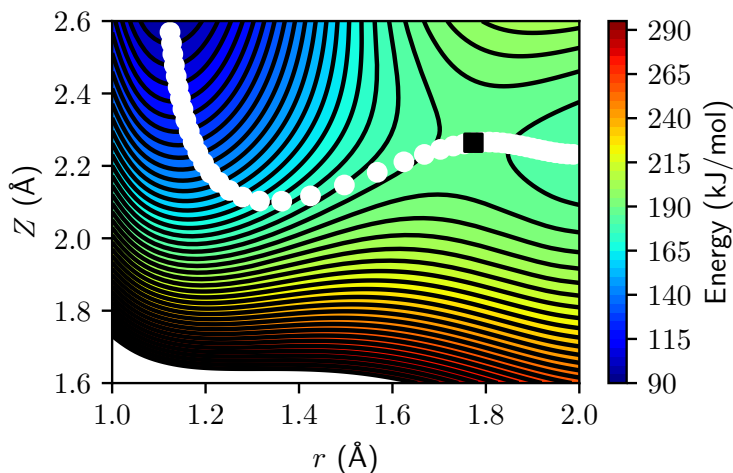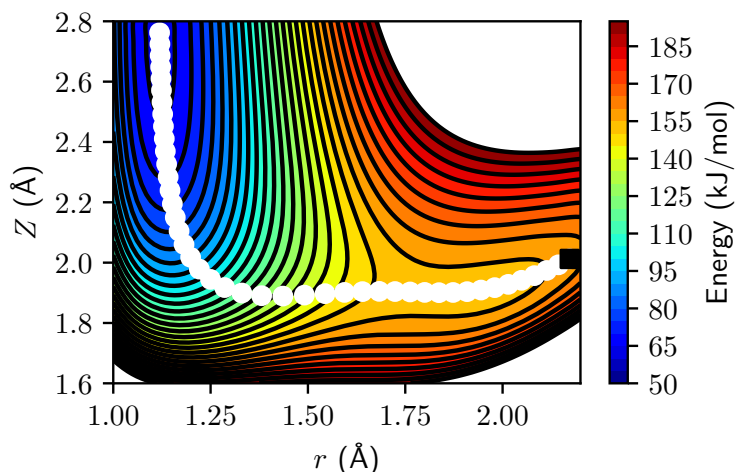
FIGURE 7.B.1: Elbow plot of methane on Cu(111) as a function of $Z$ and the distance of the dissociating CH-bond. The other coordinates of methane are kept fixed at their values at the top site C2 geometry except for the COM coordinates, which are taken such that methane is placed above the fcc site. Contour lines are drawn at intervals of 5 kJ/mol between 90 and 300 kJ/mol. The colours indicate the energy (kJ/mol) with respect to methane in the gas phase.

of methane on Cu(211) using the E/BtoB geometry is shown in Figure 7.B.2, which is similar to the MEP obtained for the EtoE geometry and on Cu(111). This can also be seen from the curvature of the MEPs on Cu(111) and Cu(211) where the $\theta$ angle was allowed to relax in Figure 7.B.3. Above the next nearest neighbour copper atom in Pt-Cu(111) the MEP is almost identical to that of Cu(111) in Figure 7.B.4. Moreover, above the Pt atom in Pt-Cu(111) the MEP is also similar to that found for Pt(111) in Figure 7.B.5, although the barrier is later than on Pt(111). Finally, the MEP on Pd(111) in Figure 7.B.6 is similar to the MEP on Pt(111).

## 7.C    Energy Transfer

The energy transfer distributions from methane to the Cu(111), Pd-Cu(111), and Pt-Cu(111) surface, with $\langle E_i \rangle = 160$ kJ/mol and $\nu_1 = 1$, is shown in Figure 7.C.1. The energy transfer from methane to Pd-Cu(111) is roughly the same as to Pt-Cu(111), whereas Cu(111) yields the largest energy transfer. Figure 7.C.2 shows the total phonon density of states (DOS) for Cu(111) and Pt-Cu(111),
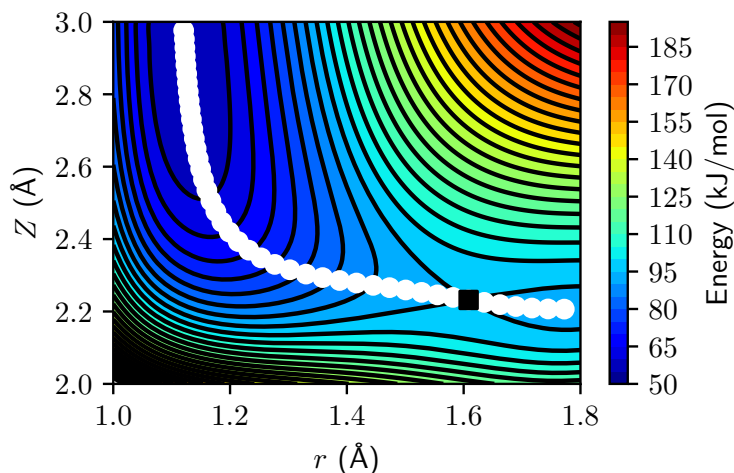
FIGURE 7.B.2: Elbow plot of methane on Cu(211) as a function of $Z$ and the distance of the dissociating CH-bond. The other coordinates of methane are kept fixed at their values at the E/BtoB geometry. Contour lines are drawn at intervals of 5 kJ/mol between 50 and 200 kJ/mol. The colours indicate the energy (kJ/mol) with respect to methane in the gas phase.
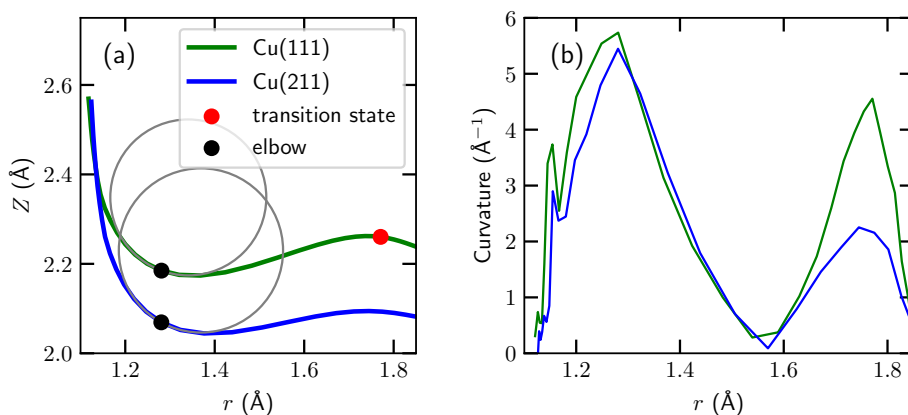


FIGURE 7.B.3: The MEP of methane on Cu(111) (green) and Cu(211) (blue) as a function of $Z$ and the distance of the dissociating CH-bond $r$ (a), and its curvature (b). The other coordinates of methane are kept fixed, except the $\theta$ angle which is relaxed, at their values at the top site C2 geometry (Cu(111)) or at the step edge EtoE geometry (Cu(211)).
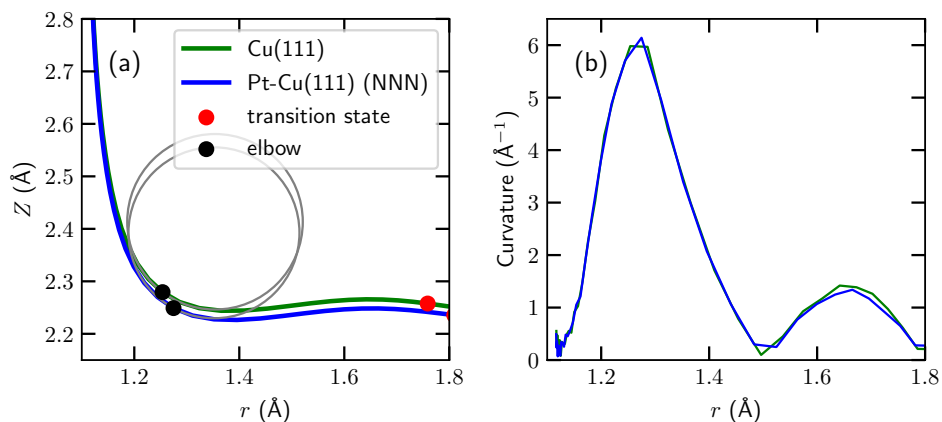
FIGURE 7.B.4: The MEP of methane on Cu(111) (green) and Pt-Cu(111) (blue, next nearest neighbour) as a function of $Z$ and the distance of the dissociating CH-bond $r$ (a), and its curvature (b). The other coordinates of methane are kept fixed at their values at the TS geometry.
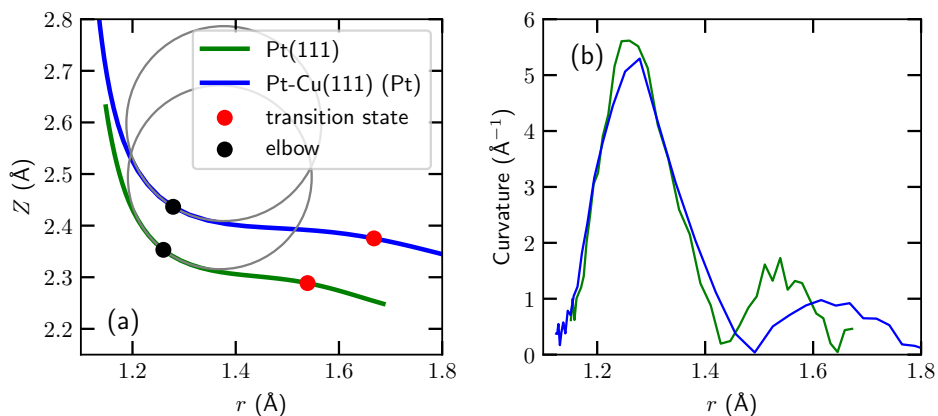


FIGURE 7.B.5: The MEP of methane on Pt(111) (green) and Pt-Cu(111) (blue, Pt) as a function of $Z$ and the distance of the dissociating CH-bond $r$ (a), and its curvature (b).The other coordinates of methane are kept fixed at their values at the TS geometry.

FIGURE 7.B.6: Elbow plot of methane on Pd(111) as a function of $Z$ and the distance of the dissociating CH-bond. The other coordinates of methane are kept fixed at their values at the TS geometry. Contour lines are drawn at intervals of 5 kJ/mol between 50 and 200 kJ/mol. The colours indicate the energy (kJ/mol) with respect to methane in the gas phase.
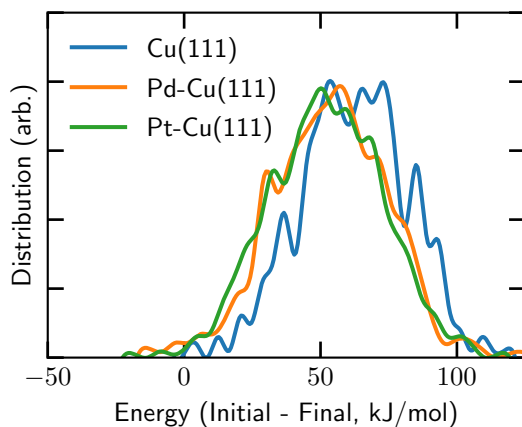


FIGURE 7.C.1: Energy transfer from methane to the Cu(111), Pd-Cu(111), and Pt-Cu(111) surface, with $\langle E_i \rangle = 160$ kJ/mol and $\nu_1 = 1$.
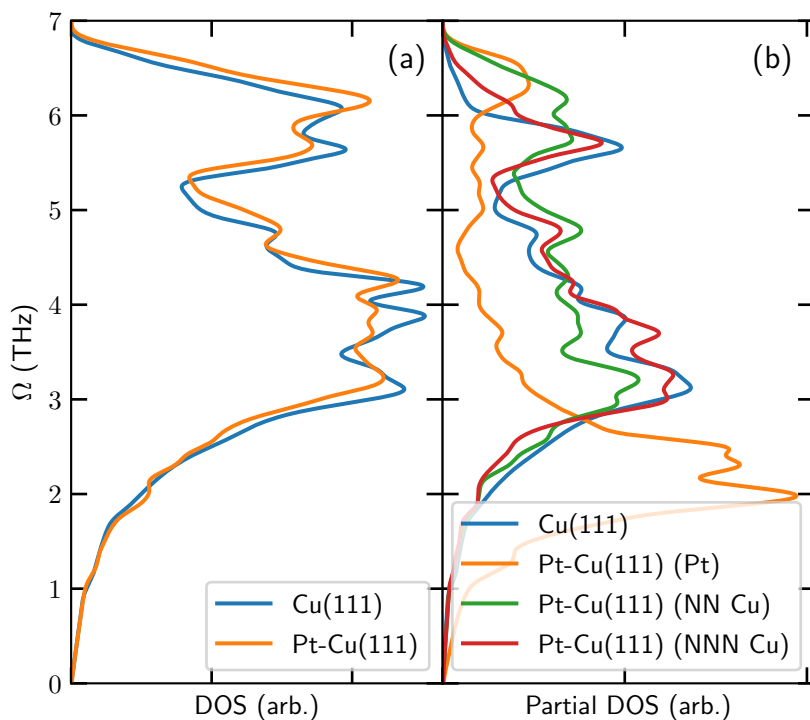
FIGURE 7.C.2: (a) Total phonon density of states (DOS) for Cu(111) (blue) and Pt-Cu(111) (orange). (b) Partial phonon DOS of the top layer Pt atom (orange), the nearest neighbour (green) and next nearest neighbour (red) Cu atoms in Pt-Cu(111), and a top layer atom in Cu(111) (blue).

which are similar. However, the partial DOS shows that the Cu top layer atoms have a similar DOS, save for the nearest neighbour Cu atom in Pt-Cu(111), whereas the partial DOS for Pt is at a lower energy.

## 7.D    Surface Atom Displacement

The distributions of the displacement in the Z direction of surface top layer atoms in Cu(111), Pt(111) and Pt-Cu(111) are shown in Figure 7.D.1. The atoms in the alloy are on average 0.05 Å lower than in pure Cu(111) and Pt(111). This corresponds well with an effectively 1.9 kJ/mol higher barrier above the Cu atoms in the alloy than on Cu(111) (see Figure 7.D.2).
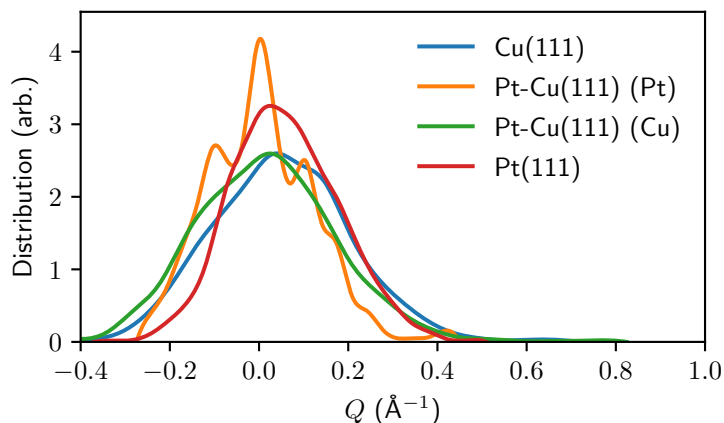
FIGURE 7.D.1: Distributions of the displacements of top layer surface atoms in the Z direction for Cu(111), Pt(111) and Pt-Cu(111) during the surface equilibration at 550 K. For Pt-Cu(111) a distinction is made between Pt and Cu.
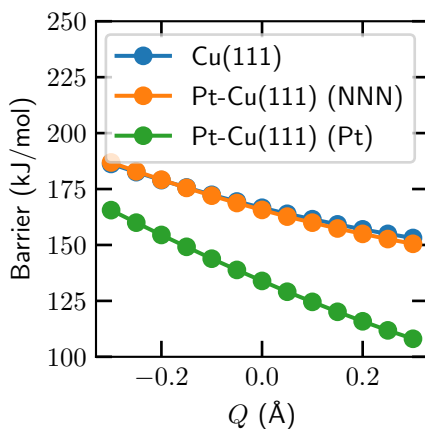


FIGURE 7.D.2: The barrier for methane dissociation on Cu(111) and Pt-Cu(111) as a function of the displacement $Q$ of the surface atom, above which methane dissociates.

# References

(1) Wei, J.; Iglesia, E. Mechanism and Site Requirements for Activation and Chemical Conversion of Methane on Supported Pt Clusters and Turnover Rate Comparisons among Noble Metals. *J. Phys. Chem. B* **2004**, *108*, 4094–4103, DOI: 10.1021/jp036985z.

(2) Jones, G.; Jakobsen, J. G.; Shim, S. S.; Kleis, J.; Andersson, M. P.; Rossmeisl, J.; Abild-Pedersen, F.; Bligaard, T.; Helveg, S.; Hinnemann, B.; Rostrup-Nielsen, J. R.; Chorkendorff, I.; Sehested, J.; Nørskov, J. K. First Principles Calculations and Experimental Insight into Methane Steam Reforming over Transition Metal Catalysts. *J. Catal.* **2008**, *259*, 147–160, DOI: 10.1016/j.jcat.2008.08.003.

(3) Li, X.; Cai, W.; An, J.; Kim, S.; Nah, J.; Yang, D.; Piner, R.; Velamakanni, A.; Jung, I.; Tutuc, E.; Banerjee, S. K.; Colombo, L.; Ruoff, R. S. Large-Area Synthesis of High-Quality and Uniform Graphene Films on Copper Foils. *Science* **2009**, *324*, 1312–1314, DOI: 10.1126/science.1171245.

(4) Losurdo, M.; Giangregorio, M. M.; Capezzuto, P.; Bruno, G. Graphene CVD Growth on Copper and Nickel: Role of Hydrogen in Kinetics and Structure. *Phys. Chem. Chem. Phys.* **2011**, *13*, 20836–20843, DOI: 10.1039/C1CP22347J.

(5) Zhang, W.; Wu, P.; Li, Z.; Yang, J. First-Principles Thermodynamics of Graphene Growth on Cu Surfaces. *J. Phys. Chem. C* **2011**, *115*, 17782–17787, DOI: 10.1021/jp2006827.

(6) Li, K.; He, C.; Jiao, M.; Wang, Y.; Wu, Z. A First-Principles Study on the Role of Hydrogen in Early Stage of Graphene Growth during the CH$_4$ Dissociation on Cu(111) and Ni(111) Surfaces. *Carbon* **2014**, *74*, 255–265, DOI: 10.1016/j.carbon.2014.03.030.

(7) Wang, X.; Yuan, Q.; Li, J.; Ding, F. The Transition Metal Surface Dependent Methane Decomposition in Graphene Chemical Vapor Deposition Growth. *Nanoscale* **2017**, *9*, 11584–11589, DOI: 10.1039/C7NR02743E.

(8) Kraus, J.; Böbel, L.; Zwaschka, G.; Günther, S. Understanding the Reaction Kinetics to Optimize Graphene Growth on Cu by Chemical Vapor Deposition. *Ann. Phys.* **2017**, *529*, 1700029, DOI: 10.1002/andp.201700029.

(9)     Tian, B.; Liu, T.; Yang, Y.; Li, K.; Wu, Z.; Wang, Y. CH$_4$ Dissociation in the Early Stage of Graphene Growth on Fe–Cu(100) Surface: Theoretical Insights. *Appl. Surf. Sci.* **2018**, *427*, 953–960, DOI: `10.1016/j.apsusc.2017.09.088`.

(10)   Kroes, G.-J. Towards Chemically Accurate Simulation of Molecule–Surface Reactions. *Phys. Chem. Chem. Phys.* **2012**, *14*, 14966–14981, DOI: `10.1039/C2CP42471A`.

(11)   Jackson, B.; Nattino, F.; Kroes, G.-J. Dissociative Chemisorption of Methane on Metal Surfaces: Tests of Dynamical Assumptions Using Quantum Models and Ab Initio Molecular Dynamics. *J. Chem. Phys.* **2014**, *141*, 054102, DOI: `10.1063/1.4891327`.

(12)   Wellendorff, J.; Silbaugh, T. L.; Garcia-Pintos, D.; Nørskov, J. K.; Bligaard, T.; Studt, F.; Campbell, C. T. A Benchmark Database for Adsorption Bond Energies to Transition Metal Surfaces and Comparison to Selected DFT Functionals. *Surf. Sci.* **2015**, *640*, 36–44, DOI: `10.1016/j.susc.2015.03.023`.

(13)   Gautier, S.; Steinmann, S. N.; Michel, C.; Fleurat-Lessard, P.; Sautet, P. Molecular Adsorption at Pt(111). How Accurate Are DFT Functionals? *Phys. Chem. Chem. Phys.* **2015**, *17*, 28921–28930, DOI: `10.1039/C5CP04534G`.

(14)   Kroes, G.-J. Toward a Database of Chemically Accurate Barrier Heights for Reactions of Molecules with Metal Surfaces. *J. Phys. Chem. Lett.* **2015**, *6*, 4106–4114, DOI: `10.1021/acs.jpclett.5b01344`.

(15)   Díaz, C.; Pijper, E.; Olsen, R. A.; Busnengo, H. F.; Auerbach, D. J.; Kroes, G. J. Chemically Accurate Simulation of a Prototypical Surface Reaction: H$_2$ Dissociation on Cu(111). *Science* **2009**, *326*, 832–834, DOI: `10.1126/science.1178722`.

(16)   Nattino, F.; Migliorini, D.; Kroes, G.-J.; Dombrowski, E.; High, E. A.; Killelea, D. R.; Utz, A. L. Chemically Accurate Simulation of a Polyatomic Molecule-Metal Surface Reaction. *J. Phys. Chem. Lett.* **2016**, *7*, 2402–2406, DOI: `10.1021/acs.jpclett.6b01022`.

(17)   Migliorini, D.; Chadwick, H.; Nattino, F.; Gutiérrez-González, A.; Dombrowski, E.; High, E. A.; Guo, H.; Utz, A. L.; Jackson, B.; Beck, R. D.; Kroes, G.-J. Surface Reaction Barriometry: Methane Dissociation on Flat and Stepped Transition-Metal Surfaces. *J. Phys. Chem. Lett.* **2017**, *8*, 4177–4182, DOI: `10.1021/acs.jpclett.7b01905`.

(18)    Groß, A. Reactivity of Bimetallic Systems Studied from First Principles. *Top. Catal.* **2006**, *37*, 29–39, DOI: `10.1007/s11244-006-0005-x`.

(19)    Ramos, M.; Martínez, A. E.; Busnengo, H. F. H$_2$ Dissociation on Individual Pd Atoms Deposited on Cu(111). *Phys. Chem. Chem. Phys.* **2012**, *14*, 303–310, DOI: `10.1039/C1CP22163A`.

(20)    Swaan, H. M.; Kroll, V. C. H.; Martin, G. A.; Mirodatos, C. Deactivation of Supported Nickel Catalysts during the Reforming of Methane by Carbon Dioxide. *Catal. Today* **1994**, *21*, 571–578, DOI: `10.1016/0920-5861(94)80181-9`.

(21)    Iglesias-Juez, A.; Beale, A. M.; Maaijen, K.; Weng, T. C.; Glatzel, P.; Weckhuysen, B. M. A Combined in Situ Time-Resolved UV–Vis, Raman and High-Energy Resolution X-Ray Absorption Spectroscopy Study on the Deactivation Behavior of Pt and PtSn Propane Dehydrogenation Catalysts under Industrial Reaction Conditions. *J. Catal.* **2010**, *276*, 268–279, DOI: `10.1016/j.jcat.2010.09.018`.

(22)    Marcinkowski, M. D.; Darby, M. T.; Liu, J.; Wimble, J. M.; Lucci, F. R.; Lee, S.; Michaelides, A.; Flytzani-Stephanopoulos, M.; Stamatakis, M.; Sykes, E. C. H. Pt/Cu Single-Atom Alloys as Coke-Resistant Catalysts for Efficient C–H Activation. *Nat. Chem.* **2018**, *10*, 325–332, DOI: `10.1038/nchem.2915`.

(23)    Tierney, H. L.; Baber, A. E.; Sykes, E. C. H. Atomic-Scale Imaging and Electronic Structure Determination of Catalytic Sites on Pd/Cu Near Surface Alloys. *J. Phys. Chem. C* **2009**, *113*, 7246–7250, DOI: `10.1021/jp809766d`.

(24)    Lucci, F. R.; Lawton, T. J.; Pronschinske, A.; Sykes, E. C. H. Atomic Scale Surface Structure of Pt/Cu(111) Surface Alloys. *J. Phys. Chem. C* **2014**, *118*, 3015–3022, DOI: `10.1021/jp405254z`.

(25)    Simonovis, J. P.; Hunt, A.; Palomino, R. M.; Senanayake, S. D.; Waluyo, I. Enhanced Stability of Pt-Cu Single-Atom Alloy Catalysts: In Situ Characterization of the Pt/Cu(111) Surface in an Ambient Pressure of CO. *J. Phys. Chem. C* **2018**, *122*, 4488–4495, DOI: `10.1021/acs.jpcc.8b00078`.

(26)    Reyes, P.; Figueroa, A.; Pecchi, G.; Fierro, J. L. G. Catalytic Combustion of Methane on Pd–Cu/SiO$_2$ Catalysts. *Catal. Today* **2000**, *62*, 209–217.

(27)    Persson, K.; Ersson, A.; Jansson, K.; Iverlund, N.; Järås, S. Influence of Co-Metals on Bimetallic Palladium Catalysts for Methane Combustion. *J. Catal.* **2005**, *231*, 139–150, DOI: `10.1016/j.jcat.2005.01.001`.

(28) Kokalj, A.; Bonini, N.; de Gironcoli, S.; Sbraccia, C.; Fratesi, G.; Baroni, S. Methane Dehydrogenation on Rh@Cu(111): A First-Principles Study of a Model Catalyst. *Journal of the American Chemical Society* **2006**, *128*, 12448–12454, DOI: 10.1021/ja060114w.

(29) An, W.; Zeng, X. C.; Turner, C. H. First-Principles Study of Methane Dehydrogenation on a Bimetallic Cu/Ni(111) Surface. *J. Chem. Phys.* **2009**, *131*, 174702, DOI: 10.1063/1.3254383.

(30) Yuan, S.; Meng, L.; Wang, J. Greatly Improved Methane Dehydrogenation via Ni Adsorbed Cu(100) Surface. *J. Phys. Chem. C* **2013**, *117*, 14796–14803, DOI: 10.1021/jp400944c.

(31) Kresse, G.; Hafner, J. Ab Initio Molecular-Dynamics Simulation of the Liquid-Metal–Amorphous-Semiconductor Transition in Germanium. *Phys. Rev. B* **1994**, *49*, 14251–14269, DOI: 10.1103/PhysRevB.49.14251.

(32) Kresse, G.; Hafner, J. Ab Initio Molecular Dynamics for Liquid Metals. *Phys. Rev. B* **1993**, *47*, 558–561, DOI: 10.1103/PhysRevB.47.558.

(33) Kresse, G.; Furthmüller, J. Efficient Iterative Schemes for Ab Initio Total-Energy Calculations Using a Plane-Wave Basis Set. *Phys. Rev. B* **1996**, *54*, 11169–11186, DOI: 10.1103/PhysRevB.54.11169.

(34) Kresse, G.; Furthmüller, J. Efficiency of Ab-Initio Total Energy Calculations for Metals and Semiconductors Using a Plane-Wave Basis Set. *Comput. Mater. Sci.* **1996**, *6*, 15–50, DOI: 10.1016/0927-0256(96)00008-0.

(35) Kresse, G.; Joubert, D. From Ultrasoft Pseudopotentials to the Projector Augmented-Wave Method. *Phys. Rev. B* **1999**, *59*, 1758–1775, DOI: 10.1103/PhysRevB.59.1758.

(36) Blöchl, P. E. Projector Augmented-Wave Method. *Phys. Rev. B* **1994**, *50*, 17953–17979, DOI: 10.1103/PhysRevB.50.17953.

(37) Methfessel, M.; Paxton, A. T. High-Precision Sampling for Brillouin-Zone Integration in Metals. *Phys. Rev. B* **1989**, *40*, 3616–3621, DOI: 10.1103/PhysRevB.40.3616.

(38) Henkelman, G.; Jónsson, H. A Dimer Method for Finding Saddle Points on High Dimensional Potential Surfaces Using Only First Derivatives. *J. Chem. Phys.* **1999**, *111*, 7010–7022, DOI: 10.1063/1.480097.

(39) Heyden, A.; Bell, A. T.; Keil, F. J. Efficient Methods for Finding Transition States in Chemical Reactions: Comparison of Improved Dimer Method and Partitioned Rational Function Optimization Method. *J. Chem. Phys.* **2005**, *123*, 224101, DOI: 10.1063/1.2104507.

(40)   Kästner, J.; Sherwood, P. Superlinearly Converging Dimer Method for Transition State Search. *J. Chem. Phys.* **2008**, *128*, 014106, DOI: 10.1063/1.2815812.

(41)   Xiao, P.; Sheppard, D.; Rogal, J.; Henkelman, G. Solid-State Dimer Method for Calculating Solid-Solid Phase Transitions. *J. Chem. Phys.* **2014**, *140*, 174104, DOI: 10.1063/1.4873437.

(42)   Transition State Tools Package for VASP https://theory.cm.utexas.edu/vtsttools/index.html (accessed 02/08/2021).

(43)   Mondal, A.; Wijzenbroek, M.; Bonfanti, M.; Díaz, C.; Kroes, G.-J. Thermal Lattice Expansion Effect on Reactive Scattering of H$_2$ from Cu(111) at T$_s$ = 925 K. *J. Phys. Chem. A* **2013**, *117*, 8770–8781, DOI: 10.1021/jp4042183.

(44)   Nattino, F.; Ueta, H.; Chadwick, H.; van Reijzen, M. E.; Beck, R. D.; Jackson, B.; van Hemert, M. C.; Kroes, G.-J. Ab Initio Molecular Dynamics Calculations versus Quantum-State-Resolved Experiments on CHD$_3$ + Pt(111): New Insights into a Prototypical Gas–Surface Reaction. *J. Phys. Chem. Lett.* **2014**, *5*, 1294–1299, DOI: 10.1021/jz500233n.

(45)   Hammer, B.; Hansen, L. B.; Nørskov, J. K. Improved Adsorption Energetics within Density-Functional Theory Using Revised Perdew-Burke-Ernzerhof Functionals. *Phys. Rev. B* **1999**, *59*, 7413–7421, DOI: 10.1103/PhysRevB.59.7413.

(46)   Perdew, J. P.; Burke, K.; Ernzerhof, M. Generalized Gradient Approximation Made Simple. *Phys. Rev. Lett.* **1996**, *77*, 3865–3868, DOI: 10.1103/PhysRevLett.77.3865.

(47)   Dion, M.; Rydberg, H.; Schröder, E.; Langreth, D. C.; Lundqvist, B. I. Van Der Waals Density Functional for General Geometries. *Phys. Rev. Lett.* **2004**, *92*, 246401, DOI: 10.1103/PhysRevLett.92.246401.

(48)   Wijzenbroek, M.; Kroes, G. J. The Effect of the Exchange-Correlation Functional on H$_2$ Dissociation on Ru(0001). *J. Chem. Phys.* **2014**, *140*, 084702, DOI: 10.1063/1.4865946.

(49)   Nattino, F.; Migliorini, D.; Bonfanti, M.; Kroes, G.-J. Methane Dissociation on Pt(111): Searching for a Specific Reaction Parameter Density Functional. *J. Chem. Phys.* **2016**, *144*, 044702, DOI: 10.1063/1.4939520.

(50)   Kroes, G.-J.; Díaz, C.; Pijper, E.; Olsen, R. A.; Auerbach, D. J. Apparent Failure of the Born–Oppenheimer Static Surface Model for Vibrational Excitation of Molecular Hydrogen on Copper. *PNAS* **2010**, *107*, 20881–20886, DOI: 10.1073/pnas.1001098107.

(51) Xie, Z.; Bowman, J. M.; Zhang, X. Quasiclassical Trajectory Study of the Reaction H+CH$_4$($\nu_3$=0,1)→CH$_3$+H$_2$ Using a New Ab Initio Potential Energy Surface. *J. Chem. Phys.* **2006**, *125*, 133120, DOI: 10.1063/1.2238871.

(52) Díaz, C.; Olsen, R. A.; Auerbach, D. J.; Kroes, G. J. Six-Dimensional Dynamics Study of Reactive and Non Reactive Scattering of H$_2$ from Cu(111) Using a Chemically Accurate Potential Energy Surface. *Phys. Chem. Chem. Phys.* **2010**, *12*, 6499–6519, DOI: 10.1039/C001956A.

(53) Nave, S.; Jackson, B. Methane Dissociation on Ni(111) and Pt(111): Energetic and Dynamical Studies. *J. Chem. Phys.* **2009**, *130*, 054701, DOI: 10.1063/1.3065800.

(54) Lee, K.; Murray, É. D.; Kong, L.; Lundqvist, B. I.; Langreth, D. C. Higher-Accuracy van Der Waals Density Functional. *Phys. Rev. B* **2010**, *82*, 081101(R), DOI: 10.1103/PhysRevB.82.081101.

(55) Klimeš, J.; Bowler, D. R.; Michaelides, A. Van Der Waals Density Functionals Applied to Solids. *Phys. Rev. B* **2011**, *83*, 195131, DOI: 10.1103/PhysRevB.83.195131.

(56) Nave, S.; Tiwari, A. K.; Jackson, B. Methane Dissociation and Adsorption on Ni(111), Pt(111), Ni(100), Pt(100), and Pt(110)-(1x2): Energetic Study. *J. Chem. Phys.* **2010**, *132*, 054705, DOI: 10.1063/1.3297885.

(57) Powell, A. D.; Kroes, G.-J.; Doblhoff-Dier, K. Quantum Monte Carlo Calculations on Dissociative Chemisorption of H$_2$ + Al(110): Minimum Barrier Heights and Their Comparison to DFT Values. *J. Chem. Phys.* **2020**, *153*, 224701, DOI: 10.1063/5.0022919.

(58) Darby, M. T.; Stamatakis, M.; Michaelides, A.; Sykes, E. C. H. Lonely Atoms with Special Gifts: Breaking Linear Scaling Relationships in Heterogeneous Catalysis with Single-Atom Alloys. *J. Phys. Chem. Lett.* **2018**, *9*, 5636–5646, DOI: 10.1021/acs.jpclett.8b01888.

(59) Park, J.; Yu, B. D.; Hong, S. Van Der Waals Density Functional Theory Study for Bulk Solids with BCC, FCC, and Diamond Structures. *Current Applied Physics* **2015**, *15*, 885–891, DOI: 10.1016/j.cap.2015.03.028.

(60) Jónsson, H.; Mills, G.; Jacobsen, K. W. In *Classical and Quantum Dynamics in Condensed Phase Simulations*; World Scientific: 1998, pp 385–404, DOI: 10.1142/9789812839664_0016.

(61) Marcus, R. A. On the Analytical Mechanics of Chemical Reactions. Quantum Mechanics of Linear Collisions. *J. Chem. Phys.* **1966**, *45*, 4493–4499, DOI: 10.1063/1.1727528.

(62)   McCullough, E. A.; Wyatt, R. E. Quantum Dynamics of the Collinear (H, H$_2$) Reaction. *J. Chem. Phys.* **1969**, *51*, 1253–1254, DOI: 10.1063/1.1672133.

(63)   Baule, B. Theoretische Behandlung Der Erscheinungen in Verdünnten Gasen. *Ann. Phys.* **1914**, *349*, 145–176, DOI: 10.1002/andp.19143490908.

(64)   Kennard, E., *Kinetic Theory of Gases: With an Introduction to Statistical Mechanics*; McGraw-Hill Book Company, Inc.: London, 1938.

(65)   Mishin, Y.; Mehl, M. J.; Papaconstantopoulos, D. A.; Voter, A. F.; Kress, J. D. Structural Stability and Lattice Defects in Copper: Ab Initio, Tight-Binding, and Embedded-Atom Calculations. *Phys. Rev. B* **2001**, *63*, 224106, DOI: 10.1103/PhysRevB.63.224106.